AGU PUBLICATIONS

JGR

Journal of Geophysical Research: Space Physics

RESEARCH ARTICLE
10.1002/2015JA021545

Key Points:
- Statistical study of LAEs over 2000-2005 using IMAGE/MENA images
- Shows that LAEs can be used to infer properties of ion precipitation regions
- Ion population generating LAEs is coincident to the plasma sheet/ring current

Correspondence to:
D. A. Mackler,
mackler.david@gmail.com

Citation:
Mackler, D. A., J.-M. Jahn, J. D. Perez, C. J. Pollock, and P. W. Valek (2016), Statistical correlation of low-altitude ENA emissions with geomagnetic activity from IMAGE/MENA observations, *J. Geophys. Res. Space Physics*, *121*, 2046–2066, doi:10.1002/2015JA021545.

Received 5 JUN 2015
Accepted 29 JAN 2016
Accepted article online 6 FEB 2016
Published online 4 MAR 2016

Statistical correlation of low-altitude ENA emissions with geomagnetic activity from IMAGE/MENA observations

D. A. Mackler[1,2], J.-M. Jahn[1,2], J. D. Perez[3], C. J. Pollock[4], and P. W. Valek[1,2]

[1]Department of Physics and Astronomy, University of Texas at San Antonio, San Antonio, Texas, USA, [2]Southwest Research Institute, San Antonio, Texas, USA, [3]Department of Physics, Auburn University, Auburn, Alabama, USA, [4]NASA Goddard Space Flight Center, Greenbelt, Maryland, USA

Abstract Plasma sheet particles transported Earthward during times of active magnetospheric convection can interact with exospheric/thermospheric neutrals through charge exchange. The resulting Energetic Neutral Atoms (ENAs) are free to leave the influence of the magnetosphere and can be remotely detected. ENAs associated with low-altitude (300–800 km) ion precipitation in the high-latitude atmosphere/ionosphere are termed low-altitude emissions (LAEs). Remotely observed LAEs are highly nonisotropic in velocity space such that the pitch angle distribution at the time of charge exchange is near 90°. The Geomagnetic Emission Cone of LAEs can be mapped spatially, showing where proton energy is deposited during times of varying geomagnetic activity. In this study we present a statistical look at the correlation between LAE flux (intensity and location) and geomagnetic activity. The LAE data are from the MENA imager on the IMAGE satellite over the declining phase of solar cycle 23 (2000–2005). The *SYM-H*, *AE*, and *Kp* indices are used to describe geomagnetic activity. The goal of the study is to evaluate properties of LAEs in ENA images and determine if those images can be used to infer properties of ion precipitation. Results indicate a general positive correlation to LAE flux for all three indices, with the *SYM-H* showing the greatest sensitivity. The magnetic local time distribution of LAEs is centered about midnight and spreads with increasing activity. The invariant latitude for all indices has a slightly negative correlation. The combined results indicate LAE behavior similar to that of ion precipitation.

1. Introduction

Intervals of increased magnetic convection transport energy, mass, and momentum through the plasma sheet. This in turn injects fresh ions into the inner magnetosphere, which (can) populate the ring current and inject energetic particles into the high-latitude atmosphere through the loss cone. Storm time ion precipitation is important to study not only just for understanding plasma sheet and ring current dynamics but also ionospheric and thermospheric responses. In the main and early recovery phase energetic precipitation contributes significantly to ring current particle and energy loss [*Kozyra et al.*, 1998a]. *Galand and Richmond* [2001] found that it also can drive nightside ionospheric conductance profiles as well as to regionally dominate the thermospheric energy budget, particularly at dusk subauroral latitudes. Other studies using in situ charged particle data from low-altitude polar orbiting platforms find that ions in the keV energy range contribute significantly as an energy source for ionization and localized heating in the subauroral and auroral zones [*Senior et al.*, 1987; *Hardy et al.*, 1989; *Newell et al.*, 1991]. The source of storm time particles is the plasma sheet associated with the ring current. A number of studies have linked plasma sheet densities to storm time enhancements of the ring current [*Jordanova et al.*, 1998, 1999b; *Kozyra et al.*, 1998a, 2002; *Ebihara et al.*, 1998; *Ebihara and Ejiri*, 2000; *Liemohn et al.*, 2001].

The exchange of energy during ion precipitation also contributes to the auroral airglow spectrum. Optical remote sensing measurements during precipitation have been made both from the ground [*Eather*, 1967; *Söraas et al.*, 1974; *Galand and Chakrabarti*, 2006] and from orbiting space platforms [*Gérard et al.*, 2001; *Galand and Lummerzheim*, 2004; *Frey et al.*, 2003; *Mende et al.*, 2003]. In *Gérard et al.* [2001] the remote sensing was from far ultraviolet (FUV) signatures from the IMAGE satellite, while the in situ data were from NASA's Fast Auroral Snapshot satellite and DMSP. The authors demonstrated the capability to differentiate the proton aurora from the electron aurora in the FUV. Proton aurora from ion precipitation is generally observed at lower latitudes or the mirror points of the closed magnetosphere.

The study of ion precipitation is not a new topic and has been measured in situ almost as long as there have been satellites. The ESRO-1 satellite (ESA) observed ions and electrons near auroral zones at altitudes of ~1500 km starting shortly after its launch in 1968. The NASA Dynamics Explorer 2 (1981–1991) observed precipitation from a near-circular orbit near 900 km. Both of these examples led to discoveries of field-aligned acceleration/precipitation [*Hultqvist*, 1971; *Winningham et al.*, 1984]. In addition to direct in situ measurements, a number of early studies were able to infer properties of precipitation regions relative to the auroral oval and diffuse aurora [*Lui et al.*, 1973; *Lui and Anger*, 1973; *Lui et al.*, 1975].

In situ ion studies to date have the inherent challenge of limited spatial and temporal coverage. Typical in situ ion precipitation data during the time range of this study (2000–2005) come from the DMSP Special Sensor Precipitating Electron and Ion Spectrometer and NOAA Total Energy Detector (TED) sensors. Both of these satellites are on a polar Sun-synchronous orbit, which means they maintain a similar local time trajectory over the course of a year. Combining all available DMSP and NOAA trajectories leaves a large local time gap directly over midnight where plasma sheet injections occur. Additionally, the period of a DMSP or NOAA satellite is roughly 100 min. For a latitudinal extent of a precipitation region near ~20°[*Pollock et al.*, 2009] this means that one in situ measuring satellite has a ~5 min pass through the high-latitude region of interest. It is desirable to attempt using imaging techniques to gain a large spatial and temporal understanding of the ion precipitation.

Storm time ion precipitation regions are spatially dynamic in response to geomagnetic activity. Prestorm precipitation patterns are found at higher L shells (larger invariant latitude), then move toward lower L shells during the main phase and back again to larger L shells with storm recovery when the ring current subsides [*Jordanova et al.*, 2001]. DMSP (F6 and F7) in situ ion precipitation data indicate significant proton flux in the afternoon and premidnight sectors, with a maximum in the Diffuse Auroral Zone equatorward of the auroral oval [*Yagodkina and Vorobjev*, 2002]. *Hardy et al.* [1989] (also using DMSP F6 and DMSP F7) observed that higher integral energy flux levels form a C-shaped distribution in magnetic local time from prenoon to premidnight. The distribution minimum (maximum) is found at prenoon (premidnight). The integral energy flux increases with *Kp* for all local times except the prenoon sector. *Hardy et al.* [1989] also showed that for increasing geomagnetic activity, there is a correlating shift in the maximum energy flux to lower latitudes while the magnetic local time location moves toward noon from the evening. Similarly, *Gussenhoven et al.* [1987] found that ion and electron high-latitude boundaries move to lower latitudes with increasing geomagnetic activity by studying ~900 boundaries observed by DMSP F6 auroral passes. Modeling studies of particle drift paths show similar trends, with higher-energy source populations drifting westward [*Korth et al.*, 1999] and higher storm activity precipitation favoring the dusk side of midnight [*Kistler et al.*, 1989].

Neutrals observed at energies significantly higher than the atmospheric thermodynamic population (few eV) are called Energetic Neutral Atoms (ENAs) and can range in energy from ~10 eV to > 1 MeV. ENAs are produced in the terrestrial magnetosphere and ionosphere when ions of sufficient energy collide with exospheric neutrals (hydrogen and oxygen) and exchange charge [*Roelof*, 1987; *Williams et al.*, 1992; *Henderson et al.*, 1997]. The once charged particles are now no longer tied to the magnetic field and can escape since the kinetic energy remaining is enough to escape Earth's gravity. The flux of ENAs escaping the magnetosphere/ionosphere is a function of an energy-dependent charge exchange cross section, the exospheric neutral density, and the ion flux [*Roelof and Skinner*, 2000].

The existence of ENAs in the terrestrial magnetosphere was first confirmed by *Meinel* [1951] from auroral substorm observations of neutral hydrogen into the upper atmosphere. Later studies began to link the charge exchange of protons with the neutral atmosphere to ring current decay and radiation belt dynamics [*Dessler and Parker*, 1959; *Hovestadt et al.*, 1972; *Moritz*, 1972]. The first direct observation of energetic neutrals found a correlation of the global decay of the ring current to ENA flux using ISEE 1 MEPI data [*Roelof et al.*, 1985]. Using the same data *Roelof* [1987] created, the first global ENA image of the ring current, concluding that the observed increase in ENA flux, is related to plasma injections associated with geomagnetic storms and substorms. Similar studies confirm that ENA flux is expected to correlate with observations in *Dst* index, indicating ring current enhancements [*Williams et al.*, 1992; *Fok et al.*, 1996]. In particular, *Jorgensen et al.* [1997] observed that 30–50 keV storm time ENA flux is proportional to the *Dst* index, particularly during early recovery. The conclusion from these studies is that the measured precipitating ions must be interacting with the neutral exosphere, creating ENAs [*Söraas et al.*, 1974; *Søraas and Aarsnes*, 1996].

Dedicated ENA imaging of the magnetosphere began with the Prelude In Planetary Particle Imaging (PIPPI) instrument on the microsatellite Astrid. *Brandt et al.* [1997] analyzed PIPPI ENA images in the energy range

of 26–52 keV from a 1000 km polar orbit and observed a good correlation between ENA flux and decreases in the *SYM-H* index. The study concluded that the ENAs are generated by precipitating ions from the inner plasma sheet (L shell of ~4–8) interacting with near-exospheric neutral atoms at an altitude of ~300–400 km. ENA imaging took a giant leap with the launch of the Imager for Magnetopause-to-Aurora Global Exploration (IMAGE) observatory [*Burch*, 2000]. IMAGE observed magnetospheric ENA flux distributions over an energy range of 15 eV to 500 keV per nucleon using three instruments: the low-energy neutral atom (LENA) [*Moore et al.*, 2000], medium-energy neutral atom (MENA) [*Pollock et al.*, 2000], and high-energy neutral atom (HENA) [*Mitchell et al.*, 2000] energy neutral atom imagers. More recently, ENA imaging has advanced further with the Two Wide-Angle Imaging Neutral-atom Spectrometers (TWINS) mission [*McComas et al.*, 2009a].

High-latitude ENA emissions between ~300–800 km are considered "low" as compared to nonprecipitating ring current "high-altitude" emissions from ~3–5 R_e. *Roelof* [1997] investigated these Low Altitude Emissions (LAE) with a simple model constructed from an assumption of a single charge exchange and exospheric oxygen neutral density computed using the Mass Spectrometer Incoherent Scatter (MSIS)-90 model [*Hedin*, 1991]. The results indicate that LAEs should be the most intense magnetospheric energetic neutral emissions. The interaction between the precipitating ions and atmospheric neutrals causes charge exchange and electron stripping. These two processes compete dynamically, producing multiple changes in charge, which in turn allows for cross-field transport and pitch angle redistribution at low altitude [*Kozelov*, 1993; *Basu et al.*, 1987; *Galand et al.*, 1998]. Low-altitude ion precipitation may undergo multiple charge exchange and electron stripping events as particles move along the high-latitude magnetic field path toward the mirror point. Particles spend some of their time charged and some of their time as a neutral [*Galand and Richmond*, 1999; *Roelof and Skinner*, 2000; *Brandt et al.*, 2001a]. This concept lead to the development of a multiple-collision "thick-target approximation" (as opposed to a single collision "thin-target") model of the high-latitude ion precipitation interacting with the neutral oxygen exosphere at altitudes of several hundreds of kilometers [*Bazell et al.*, 2010]. The current thought is that the LAE emission region altitude comes from a narrow range (tens of kilometers) which can change dynamically with changing magnetic and solar conditions [*Roelof*, 1997].

Recent studies of the LAEs revealed interesting storm time features that reinforce past observations and open new questions. *Pollock et al.* [2009] computed the pitch angle and invariant latitude distributions of MENA neutral atom images and found a strong connection to in situ high-latitude precipitation patterns. This was studied further by *Bazell et al.* [2010] where the thick-target approximation is used to compute the precipitating ion pattern from TWINS images. The resulting high-latitude spatial distribution of ions agreed with DMSP in situ data. *Valek et al.* [2010] compared the low- and high-altitude ENA emissions from a moderate storm near the beginning of solar cycle 24 (22 July 2009) seen in TWINS images. The LAE was observed first and brightest during the main phase, then diminishing in intensity during recovery to be only as bright as the bulk Ring Current Emission. This was later confirmed using a deconvolution technique to extract ion information from TWINS ENA images during the same storm [*Perez et al.*, 2012].

Ilie et al. [2013] studied the sensitivity of ENA generation with the geocoronal hydrogen density. They used five geocoronal neutral models along with the Hot Electron and Ion Drift Integrator (HEIDI) ring current model to simulate the 22 July 2009 geomagnetic storm. Results of the simulation were compared with TWINS ENA observations and indicate that the neutral hydrogen geocorona may play a significant role in ring current decal and recovery. *Søraas and Sørbø* [2013] looked at protons and ENAs near the proton oval during the Halloween superstorm on 29 October 2003 using Medium Energy Proton and Electron Detector (MEPED) data from NOAA POES 15. They found that the precipitation of protons lost to the atmosphere happened simultaneously with the buildup of the ring current. They conclude that the proton aurora during a geomagnetic storm is not from the ring current loosing particles but as a result of it filling up. *Colier et al.* [2015] reported on the recent VISIONS sounding rocket observations of a spatially localized filamentary ENA source near the polar cap boundary. They found that in the energy range of the study (peaks at ~100 eV) the ENA source is from downward and transverse traveling ions from an altitude range of 300–600 km.

In this study we present configuration and velocity space distributions derived from the MENA instrument on the IMAGE satellite. The distributions are compared with prior studies to validate the accuracy of the image analysis method and then correlated with changes in geomagnetic activity using the *AE*/*Kp*/*SYM-H* indices. The intent of the study is to show that images of neutrals created by charge exchange can be used as a proxy for ion precipitation regions, particularly in flux and spatial extent.

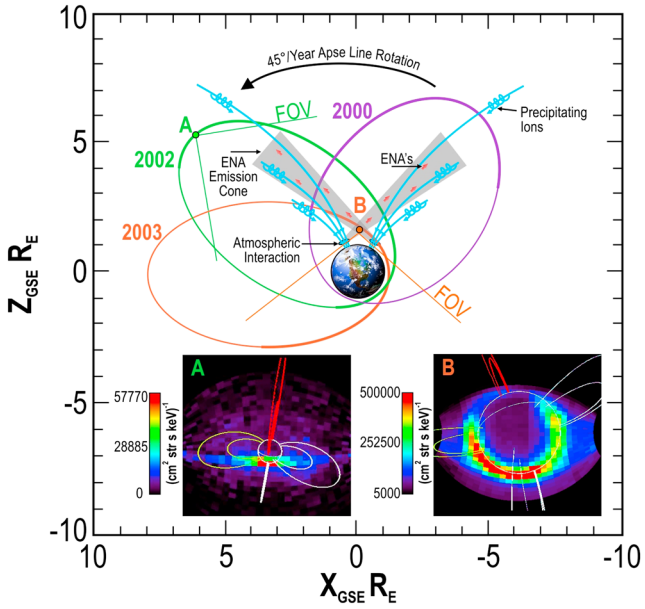

Figure 1. Cartoon illustrating the concept of the Geomagnetic Emission Cone (GEC) in relation to the IMAGE orbit and MENA ENA images. Observations from further out (2002 example) see a narrow beam of ENAs from the opposite hemisphere. Closer observations (2003 example) see a collective of multiple emission regions extending over a wide range of local times. The GEC is the highly anisotropic neutral emission escaping from the inner magnetosphere and observed remotely.

2. IMAGE MENA LAE Data and the Geomagnetic Emission Cone

The launch of NASA's IMAGE mission provided for the first time the simultaneous imaging of magnetospheric dynamics using a suite of instruments over a wide range of energies. The mission epoch (2000–2005) during the declining phase of solar cycle 23 was an interesting time to study the inner magnetospheric response to geomagnetic storms due to a large number of strong storm time activity. IMAGE flew in an inertial orbit whose trajectory traveled over all local times twice per year. The orbit was highly elliptical with a perigee altitude of ~1000 km out to apogee at ~7.2 R_e. The slower orbital velocity near apogee allows IMAGE to obtain multiple images during a geomagnetic storm time, which may last many hours. The line of apsides of the orbit rotated ~45°/year, allowing multiple vantage points (see Figure 1; the colored ellipses represent the rotation of the orbit; thicker regions of the orbit indicate when data are available).

The data used in this study come from the Medium Energetic Neutral Atom (MENA) imager on board IMAGE. MENA is a 1-D neutral atom imaging slit camera that uses a position sensitive anode to determine the incoming ENA direction (elevation) within the combined field-of-view (between three sensor heads) of 140°. The 2 min spin of the IMAGE satellite then completes the second dimension of the MENA neutral atom image (azimuth). MENA can measure combined hydrogen and oxygen neutrals in the energy range of ~1–30 keV/amu, giving it an advantage toward studying plasma sheet particles.

The concept of an "ENA Emission Cone" was introduced in *Pollock et al.* [2009] to illustrate how the remote viewing of LAE events are dependent on observation location. It was later termed the Geomagnetic Emission Cone (GEC) to emphasize the source of neutrals. At the emission region the LAE ENA velocity space distribution is expected to be locally symmetric (but not fully isotropic) with respect to the local magnetic field due to a gyrotropic ion distribution. When observed remotely the velocity space appears highly anisotropic and at roughly mirroring pitch angles. Furthermore, the magnetic local time (MLT) coverage seems limited in extent by the location of the satellite. This is mathematically represented in *Bazell et al.* [2010] with the development of an "emissivity function" using ion precipitation. The function has no a priori dependence in MLT or L shell, and it has a property that a LAE can only appear in a produced ENA image where the emissivity function is nonzero.

In Figure 1, the blue lines represent a dipole field and the spiraling path of ions toward a polar mirror point. If the point is below the oxygen exobase then the loss cone begins to empty. Pitch angles greater than 90°

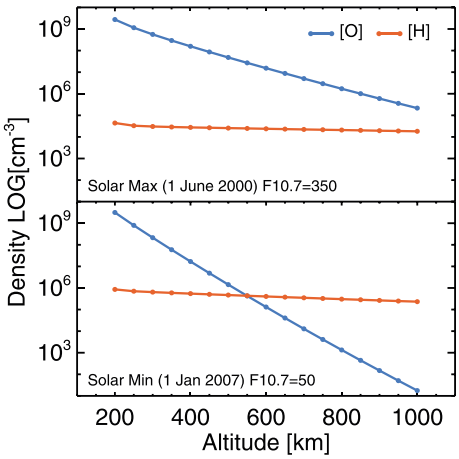

Figure 2. Two MSIS-90 runs simulating conditions for solar (top) maximum and (bottom) minimum. The intersection between the [H] and [O] lines represent the altitude where the oxygen number density begins to dominate and charge exchange collisions occur more frequently. The altitude ceiling in the figure is a limitation of the MSIS-90 model. (http://omniweb.gsfc.nasa.gov/vitmo/msis_vitmo.html)

have already mirrored, and the likelihood that they will charge exchange above the oxygen exobase is less than below it. Pitch angles less than 90° have yet to mirror. If charge exchange occurs before the mirror point, the velocity vector will bring the new neutral further into the atmosphere. Pitch angles near 90° have a significant chance to charge exchange and have a velocity relative to the magnetosphere conducive to escape. In addition, a neutral has a smaller chance of encountering a secondary collision if it travels through a less dense part of the geocorona. It is anticipated that this will result in a pitch angle distribution centered slightly above 90°.

The location of the observing platform relative to the GEC determines what kind of information can be obtained about the LAE. Observations from just one vantage point will not give sufficient information about the source latitude and local time. For a case study the limitations of the GEC would prevent a full understanding of the LAE event, and more comprehensive data sources would be needed. For a statistical approach, however, sampling multiple images over a range of MLTs and distances allows a cumulative view of LAEs. *Goldstein et al.* [2013] used TWINS images from 6 April 2010 to determine the geophysical position of LAE regions. The near-dusk region was observed from the opposite hemisphere and was wide in local time (8.4–9.2 h), at a narrow range in magnetic latitude (67°–74°), and pitch angles slightly larger than 90° (112°–116°). The observations discussed in *Goldstein et al.* [2013] are consistent with the concept of the GEC.

3. ENA Image Analysis

In the bottom left and right of Figure 1 are two sample ENA images from the MENA instrument. The white circle in the middle of the image represents the limb of the Earth, and the other lines indicate the magnetospheric dipole field lines at L shells of 4 and 8. The red L shells are at MLT of 1200, and the yellow are at 1800. The pixel color represents the intensity of the line-of-sight integrated ENA count rate, converted to differential directional number flux. The "*x*" dimension of an image is the instrument field of view (elevation), and the "*y*" dimension is the spacecraft spin (azimuth). The strategy to obtain configuration and velocity space information from a pixel on an image is to assume that the emission of LAEs come from a thin spherical shell of radius $R_e + h_{em}$ centered on the Earth, where h_{em} is the emission region altitude (for the purposes of this paper the subscript "em" will be used to refer to the fixed emission region). The coordinates of each pixel are computed and used to find values of MLT, invariant latitude (IL), and pitch angle (PA) for each pixel. The exact altitude of this spherical shell is not well understood, and a range of values have been used in previous studies.

The region of the atmosphere currently thought to be responsible for the creation of LAEs is where the number density of neutral oxygen begins to overtake that of hydrogen [*Roelof*, 1997; *Galand and Richmond*, 1999]. To estimate where this happens, we use the MSIS-90 model [*Hedin*, 1991] to see what the number densities are for oxygen and hydrogen during times near solar maximum and minimum (Figure 2). In this simple study we can see that the altitude where [O] ≈ [H] is highly dependent on the solar conditions and may vary over a few hundred kilometers. The resulting GEC should have a variable source altitude that is a function of the vertical neutral density profile. MENA images are obtained from distances of thousands to tens of thousands of kilometers. An uncertainty in emission altitude of a few hundred kilometers is not likely to greatly affect the results. A fixed value of 650 km is set as the LAE altitude based on the work of *Pollock et al.* [2009].

MENA is unable to discern between neutral hydrogen and oxygen. The objective of the study is to evaluate spatial-temporal properties of precipitating ions (mostly hydrogen) and not the composition of precipitation. Therefore, only the lower energy range (~1–12 keV/amu) of the instrument is used. Using higher energies

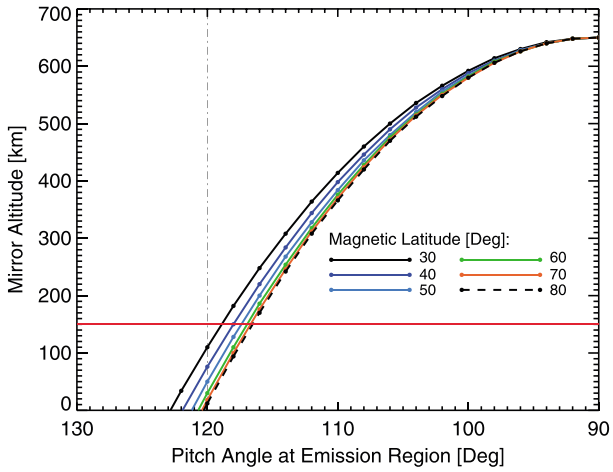

Figure 3. Observed pitch angle for particles mirroring ($\alpha = 90°$). The observed pitch angle at $h_{em} = 650$ km are the values on the x axis. The horizontal red line indicates a lower altitude limit. Only observed pitch angles relating to a mirror point above this line are accepted. This graphical result of the model developed in section A3 is symmetric about 90°.

increases the chance that the ENAs are from low-energy [O]. This also increases the counting statistics for LAE regions in an image. However, this limitation also means that careful consideration is required when the source population is discussed.

To prevent false positive and negative LAE identifications, each MENA image is viewed manually in two stages to identify those showing a LAE signature. The first stage flags every image that shows possible signs of a LAE without prior knowledge of storm activity. Distributions are made of the PA/MLT/IL values for every pixel intersecting $R_e + h_{em}$ for every image in this LAE data set (see sections 3.1 and 3.2 for details). In the second stage the computed distributions of PA/MLT/IL versus differential directional energy flux are compared to the LAE images to further filter out false positives. Each of the three PA/MLT/IL distributions are plotted with the pixel differential directional energy flux as the magnitude. If the location of the most intense pixel in PA/MLT/IL is not roughly consistent to the apparent position of that pixel in the image, that image is removed from the LAE data set.

3.1. Image Batch Processor

The job of the batch processor is to collect all spatial and magnetic field information for every valid pixel in a LAE image and save that data for further processing (see Appendix section A1 for details). Over a single spin of IMAGE the MENA instrument will integrate counts per azimuth bin (4°) for a little more than a second (1.33 s). During that time (combined with the binning in the elevation direction) there is a spatial uncertainty as to where in that pixel the ENA flux maps to. To gain some information about the extent of this uncertainty, each pixel is sampled at five locations; each corner and the center. To eliminate unneeded computation, only those pixels in an image that have one corner within $R_e + h_{em}$ are considered.

While the altitude of the emission region can be quite variable, it is thought that at a specific time, the extent in altitude where LAEs are generated is limited. The batch processor fixes this region to a hemispherical shell projected from Earth center toward the spacecraft (S/C) at an altitude of $R_e + h_{em}$. The spherical coordinates of a pixel on the hemispherical shell are found by first creating a new user defined coordinate system. The Geocentric Pixel Projection (GPP) coordinates has the "Z" component centered on the Earth and pointing

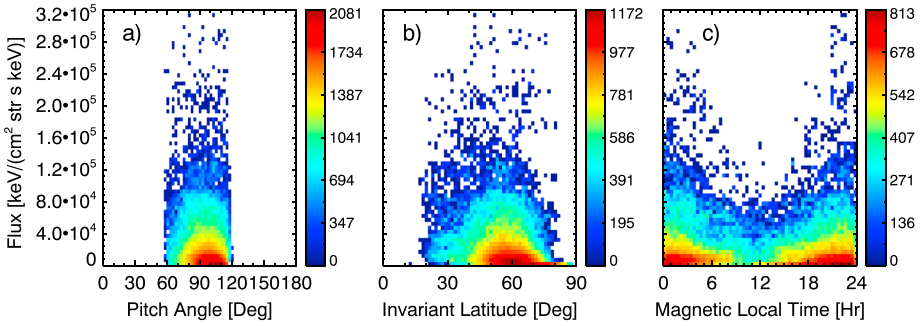

Figure 4. The (a) pitch angle, (b) invariant latitude, and (c) magnetic local time distributions derived from Low Altitude Emission pixels (mean value) observed in MENA images over 2000–2005. The magnitude is in distance corrected differential directional energy flux. The color bar represents the number of pixels included in a single bin.

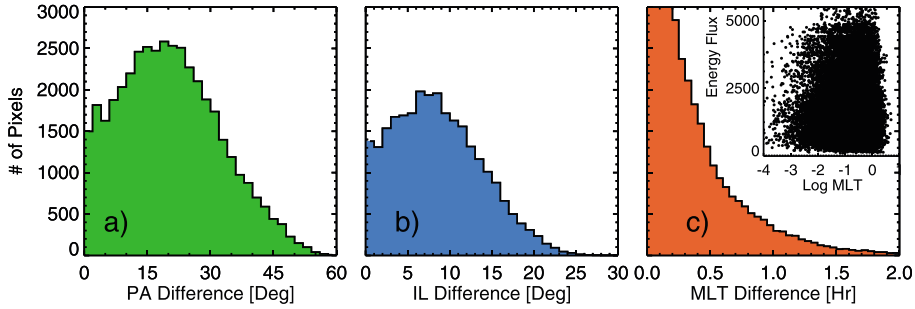

Figure 5. LAE pixel difference (maximum minus minimum) histograms for the data in Figure 4. The difference distributions illustrates the ability of the data to properly resolve anticipated changes in the ion precipitation region over altitude (pitch angle (PA)) and location (magnetic local time (MLT) and invariant latitude (IL)).

toward the S/C. The "*Y*" component is aligned with the S/C spin vector, and "*X*" completes orthogonality. The two spherical angles are called eta $\rightarrow \eta$ (colatitude) and epsilon $\rightarrow \epsilon$ (longitude or ratio between azimuth and elevation).

It is desired to have these pixel coordinates in a more universal system. A rotation matrix is applied to the GPP coordinates, eventually converting them to the solar magnetic (SM) system. The magnetic field vector for each of the five points in a pixel is then computed using the point coordinates and the International Geomagnetic Reference Field (IGRF-9) [*Macmillan et al.*, 2003] magnetic field model. The emission region for this analysis is fixed to 1.1 R_e. While the Earth magnetic field can reasonably be assumed to be a dipole out to $\sim 6R_e$ [*Parks*, 2004], we use the IGRF at this step to improve the accuracy of the magnetic field which will be used to compute the pitch angle (see section 3.2).

3.2. Image Postprocessor

The postprocessor reads in the pixel point coordinate information collected by the batch processor and computes desired physical values (see Appendix section A2 for further details). Again, to reduce unneeded computation, only points within $R_e + h_{em}$ are used for further processing such that each valid pixel may have 1–5 points. SM coordinates are used to find the MLT and magnetic latitude (ML). The assumed emission altitude combined with the ML is used to get the L shell value at a point, which leads right to the IL. The inner product between the magnetic field and the vector from the point coordinate to the S/C gives the pitch angle of observed ENAs. All valid points per pixel are used to find the maximum, minimum, mean, and median values in FLUX/PA/MLT/IL for a pixel.

The pixel values are then put through a "pitch angle filter" (Figure 3) to eliminate unrealistic values. Too low or high of pitch angles come from an unrealistic mirror altitude. Low estimates put the proton aurora altitude at around 150 km; this is the lower limit we set for the mirror altitude. A simple model based on the first adiabatic invariant and the assumed emission region (see Appendix A3) determines the altitude where the computed mean pitch angle becomes 90°. Pixels that have a mirror altitude above 150 km are used for further study. Figure 3 illustrates the developed model for different MLs. Using this filter effectively gives a more realistic pitch angle range of ~60°–120° = (±30° about 90°).

At this point the processed image has PA/MLT/IL and flux information for all pixels mapped to within $R_e + h_{em}$. However, an LAE is regionally limited in MLT and IL; therefore, using all pixels within Earth's limb is not useful for this study. Furthermore, there are images from the Northern and Southern Hemispheres. It is desired to remedy the two of these issues for clarity. The IL and PA of the Southern Hemisphere images are converted (absolute value of IL and "flip" the pitch angle about 90°) to make all values comparable. Pixels with a value greater than 0.6 times the maximum (= will be considered a LAE pixel) are used for further analysis. This reasonably extracts only those pixels that contribute significantly to a LAE signature. The data are now filtered to just LAE pixels rather than an entire image containing ENA pixels.

4. LAE Pixel Distributions

Figure 4 is the PA/MLT/IL distribution results of the analysis process described in sections 3.1 and 3.2. All six years of MENA LAE pixel data are combined, and the Southern Hemisphere data are folded into the Northern

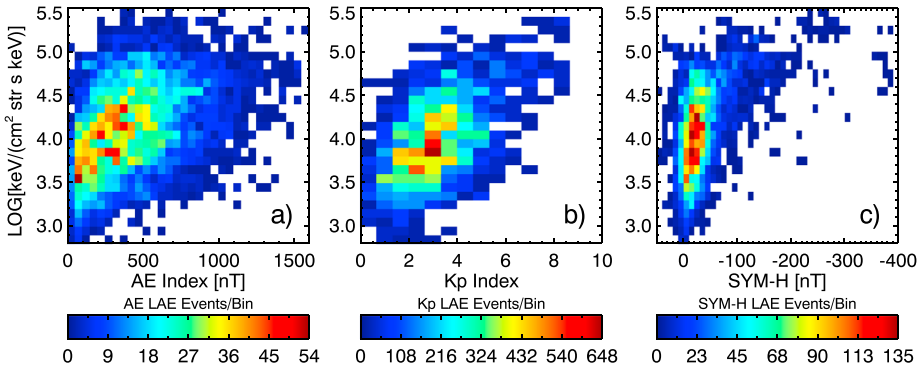

Figure 6. Differential directional energy flux of LAE pixels with (a) *AE*, (b) *Kp*, (c) and *SYM-H* indices. While all show a positive correlation, the *SYM-H* response shows a rapid increase in flux with increasing ring current activity.

Hemisphere data (as discussed in section 3.2). The color bar numbers indicate the number of pixels per bin in the color plot. Magnitude units in the *y* axis are differential directional energy flux over 1–12.1 keV/amu.

In this statistical study many images taken at varying locations along the IMAGE orbit are evaluated together. In a single image it is difficult to determine if a change in intensity is due to the change in the distance to the emission source or if the intensity of the emission source itself changes. It is desirable to do some type of distance correction such that different observation locations can be compared. Most ENA/LAE studies do not use such a correction; either they use single-image case studies or the time period of the study is small enough to assume small changes in distance. Although this correction has been done in previous studies it is not trivial. *Goldstein et al.* [2013] used a geometric correction factor between the TWINS image angle pixel resolution and an estimate of the scale size of the emission region using high spatial resolution Astrid images to solve this problem.

In this work there are images further out where the emission source region is smaller than a MENA pixel, and the LAE can be treated as a point source which drops in intensity with $1/R^2$. However, if an image is measured closer in the MENA, pixel size becomes increasingly smaller compared to the local magnetospheric geometry, and a greater extent of the GEC is observed (see the MENA image labeled "B" in Figure 1). In these cases the intensity may scale as $1/R$ for extended "line-like" emission regions or even just one for images where blocks of pixels make up a LAE. To complicate matters further, we are assuming a fixed emission altitude while in reality it is dynamic, possibly changing hundreds of kilometers depending on solar and magnetic conditions. Due to the highly eccentric orbit most of the images are when IMAGE is far enough out such that it is reasonable to assume a point source.

For this study we are using a $1/R^2$ correction to every LAE image where R is the distance from the source region and the satellite location. While we will not be able to say absolutely what the actual intensity of the source emission is, we will be able to qualitatively compare all images together. For the rest of this paper when we discuss differential directional energy flux (or just flux) it infers that the intensity has been distance corrected.

Results from the initial processing of the data indicate reasonable distributions that agree with prior studies [*Søraas and Aarsnes*, 1996; *Pollock et al.*, 2009; *Buzulukova et al.*, 2013; *Vorobjev and Yagodkina*, 2014]. The combined pitch angles appear centered slightly above 90°, which for nearly mirroring neutrals escaping the atmosphere is expected. Over multiple storms and observational distances a large range of latitudes contribute to the total distribution. At a distance of 7 R_e the Earth limb has an angular extent of ~20° compared to the largest pixel dimension of 5°. When a pixel is scaled to midlatitudes it covers ~8°–9° IL (Figure 5). Despite this we still observe latitudes centered slightly below 60°(L shell < 4), which is a reasonable location for ion precipitation from the ring current. The local time coverage shows LAE pixels on the dayside, which while much less probable is still possible. However, the total distribution is roughly centered slightly on the dusk side of midnight, which is consistent with the source population coming from the plasma sheet. These results indicate that the analysis method used to compute real values from ENA images is analogous to ion precipitation configuration and velocity space distributions.

It is desirable to evaluate the ability to resolve spatial features. In other words, is the uncertainty in the emission per pixel small enough to be able to tell something about the IL, MLT, and altitude of the ion/atmosphere

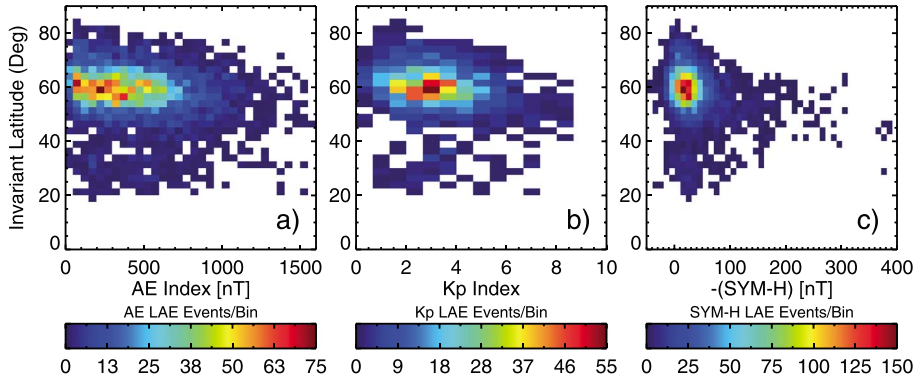

Figure 7. Invariant latitude of LAE pixels correlated with (a) *AE*, (b) *Kp*, (c) and *SYM-H*. All three indices show a downward trend in IL for increasing activity. However, the *SYM-H* response appears the most sensitive.

interaction region? Figure 5 shows histograms of the pixel difference (maximum minus minimum). The *y* axis is the number of pixels per histogram bin. The peak difference in pitch angle reflects an altitude uncertainty of about 200 km (see Figure 3). This means that our emission region lies in a range of 550–750 km. The invariant latitude is the most sensitive to pixel uncertainty, yet the IL difference distribution shows a peak (Figure 5b) below ~10°latitude, which is within the extent of the range of observed ion precipitation. Pixel local time uncertainty is least significant. The estimated arc length in local time of a pixel taken from a 1000 km pass is ~0.05 h, while at 7 R_e the local time of a pixel is ~2.2 h. The inset of Figure 5c is the log of the local time difference, showing that the distribution has a peak near 0.01 h.

5. Geomagnetic Correlations

To ascertain if ENA images respond similarly to ion precipitation during storm times, the computed LAE pixel information is correlated with geomagnetic indices. In particular, we consider *AE*, *Kp*, and *SYM-H*, using all LAE data a priori of knowledge of storm times. This means that there are LAE data available during storm time intervals as well as quiescent times in *SYM-H*. *AE* and *SYM-H* data are binned (along with the LAE data) in a 10 min time cadence, while *Kp* is kept at its original 3 h interval.

Figures 6 and 7 respectively show the correlations of differential directional energy flux and IL with *AE*/*Kp*/*SYM-H*. The negative of the *SYM-H* index is used in these figures to reduce confusion, such that a larger positive value plotted reflects a stronger storm. The MLT change with *AE*/*Kp*/*SYM-H* (Figure 8) does not follow a statistical correlation; however, for completeness and comparison it will be discussed alongside the flux and IL.

All three indices show an increase in flux (Figure 6) and a decrease in latitude with increasing activity (Figure 7). The local time coverage of LAEs shows an expansion in MLT as *AE*/*Kp*/*SYM-H* increases, centered slightly dusk

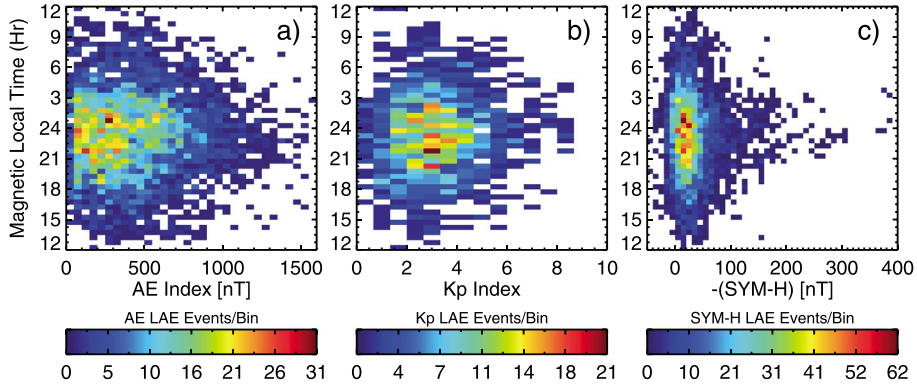

Figure 8. Magnetic local time correlation of LAE pixels with (a) *AE*, (b) *Kp*, (c) and *SYM-H*. All three indices increase in MLT extent over increasing activity until statistics eventually "pinches" the distribution at larger index values. Over the three the *SYM-H* shows a more sensitive response at lower values.

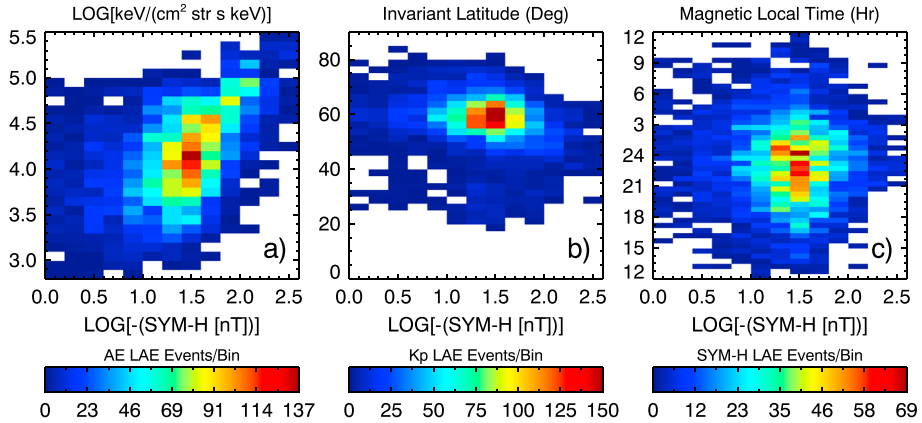

Figure 9. (a) Differential directional energy flux, (b) invariant latitude, (c) and magnetic local time correlation to the log of the *SYM-H* index. For increasing activity the flux increases, IL decreases, and the MLT spreads centering roughly premidnight.

of midnight (Figure 8). The local time expansion eventually stops and reduces as the availability of data at higher activity levels decreases.

Out of the three indices, the *SYM-H* response of differential directional energy flux and IL is the most nonlinear. Figure 9 isolates the flux, IL, and MLT to just *SYM-H*, where the *x* axis has been plotted in log scale. The large number of events (pixels) seen as yellow to red bins for low *SYM-H* values in Figures 6–9 are due to the number and intensity of storms during the period of study. About 70% (out of ~90) identified storms have a minimum *SYM-H* value of −150 nT or higher (end of main phase), leading to a greater amount of pixels over the range 0 nT > *SYM-H* > −150 nT.

The Pearson Correlation Coefficient (PCC) for the differential directional energy flux with *AE* and *Kp* (Figures 6a and 6b) are 0.388 (15%) and 0.564 (32%), respectively. However, if the log of *AE* is used, the coefficient increases to 0.432 (18.7%). The percentile added to the coefficient is a statistical measure of the fraction of the variability between the two values that are correlated. Keeping the convention in Figure 9, the PCC for the flux with the log of *SYM-H* is 0.531 (28%). Similarly, the PCC is computed for the IL correlated with *AE*/*Kp* and the log of *SYM-H* resulting in values of −0.186 (3.5%), −0.207 (4.3%), and −0.209 (4.4%). While the IL correlations are statistically weak, the trend of decreasing latitude with increasing activity is obvious over all indices. Similarly, the flux response shows a definite increasing trend with all three indices with a positive, but not strong, correlation.

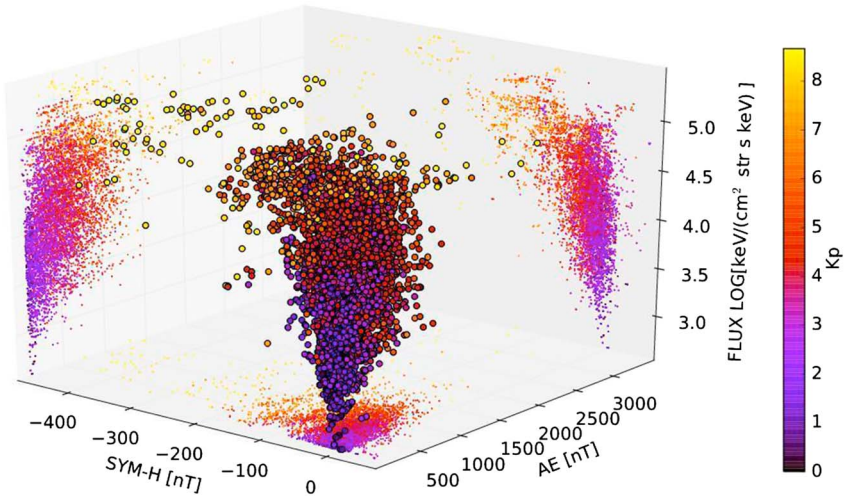

Figure 10. Three-dimensional plot showing the *AE*/*SYM-H*/FLUX distributions together. The data point color indicates the intensity of the *Kp* index.

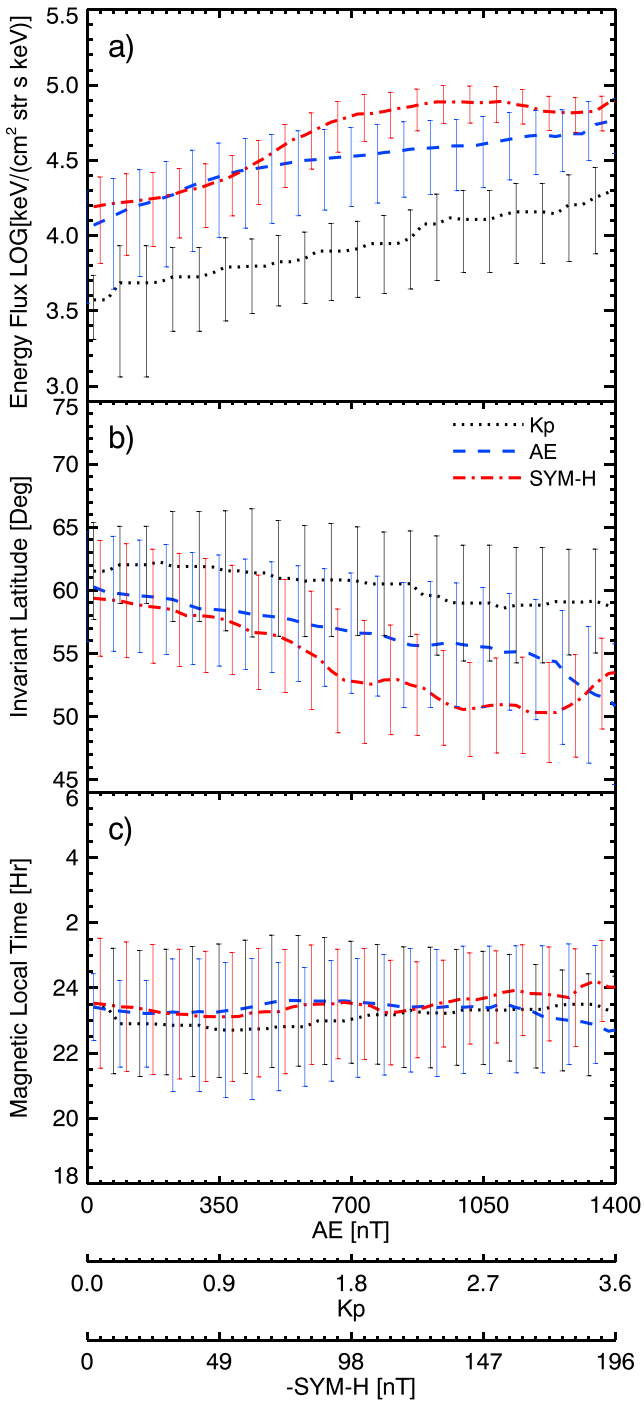

Figure 11. (a) Differential directional energy flux, (b) invariant latitude, (c) and magnetic local time trendlines from Figures 6–8 using mean values as a function of geomagnetic activity. The *SYM-H* index shows a more significant response in flux and IL compared to *AE* and *Kp*. All three geomagnetic indices show an offset in MLT toward premidnight fairly constant over all activity.

It is reasonable to anticipate that the differential directional energy flux in ion precipitation will increase along with higher geomagnetic activity for all three indices. The LAE response shows a similar trend, particularly with *SYM-H*. This indicates a possible positive correlation of LAE flux with the storm time ring current. The energy range of neutrals used in this study is too low to make a conclusion that the source population contributing to charge exchange is from the symmetric ring current.

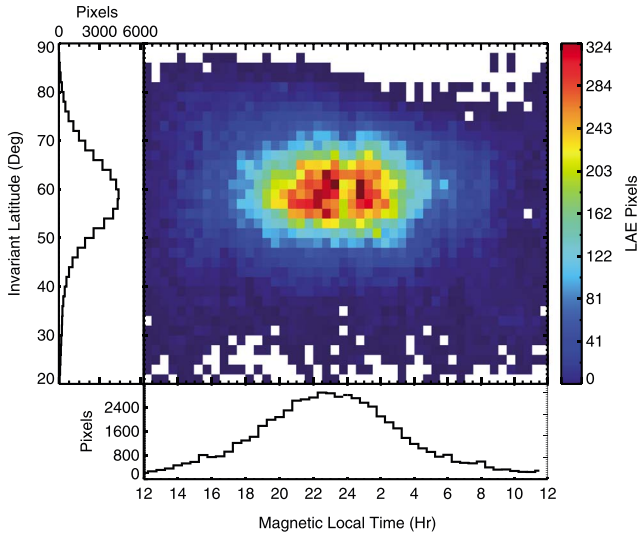

Figure 12. Magnetic local time and invariant latitude correlation of LAE pixels. The MLT is roughly centered just before midnight, and the IL peaks slightly below 60° latitude.

All trapped particles in the magnetosphere in some spatial extent add to the ring current. However, only ions with energies of ~10 keV to a few hundreds of keV comprise the significant portion of the total current density [*Daglis et al.*, 1999; *Williams*, 1987]. Therefore, it is possible that a fraction of the same particles injected from the plasma sheet forming the ring current are charge exchanging and being lost as LAEs.

As a further investigation into the correlation of the differential directional energy flux with the indices we can look at how the three relate together using multiple correlation analysis. Figure 10 shows a single view of a 3-D visualization of the flux with the three indices. The data point color is the *Kp* index. The combined distribution fans out in *SYM-H* and *AE* with increasing *Kp*. A larger number of high flux data points follow the trend toward more negative *SYM-H* values. This further reinforces the concept that the flux response to *SYM-H* is the most nonlinear out of the three. For the multiple correlation the *AE*/*Kp*/*SYM-H* values are the independent variables, and the flux is the dependent variable. The combined multiple correlation coefficient of the three independent variables to the flux is 0.584 (34%).

To clarify possible trends in the data presented in Figures 6, 7, and 8, we calculate the means of differential directional energy flux, IL, and MLT as a function of the various activity indices. Figure 11 is the result of this trendline for the flux, IL, and MLT, respectively. The error bars are determined using the standard deviation of each vertical distribution.

Both substorms and geomagnetic storms contribute to injections of ions into the high-latitude thermosphere, potentially leading to charge exchange. The change in the differential directional energy flux trendline reinforces that seen in Figure 6, where there is significantly a greater contribution from ring current associated activity. The latitude trendline for the *SYM-H* correlation is both smaller in magnitude and decreases faster than the other two indices. This decrease in latitude of LAEs begins near the same −50 nT level in *SYM-H*, indicating that the increase in flux and decrease in latitude are related. The local time trendlines of all three indices are similar (within ~1 h) with a slight offset duskward from midnight.

6. Emission Source Region

In addition to correlating with geomagnetic activity, the LAE active source region should also show a similar spatial trend to precipitation locations. Figure 12 is the MLT/IL distribution of LAE pixels, binned 0.50 h in MLT and 2° in IL. The local time of the majority of the pixels appear slightly duskward of midnight with a latitude range of ~50°–70°. The pattern of LAE pixels in Figure 12 is indicative of plasma sheet particles migrating into the nightside inner magnetosphere.

Figure 13 splits the LAE pixels from Figure 12 into times of stronger (<−100 nT) storms and weaker storms. As was seen in Figure 7, the IL is observed to decrease slightly with increasing *SYM-H* activity. Figure 13 shows a

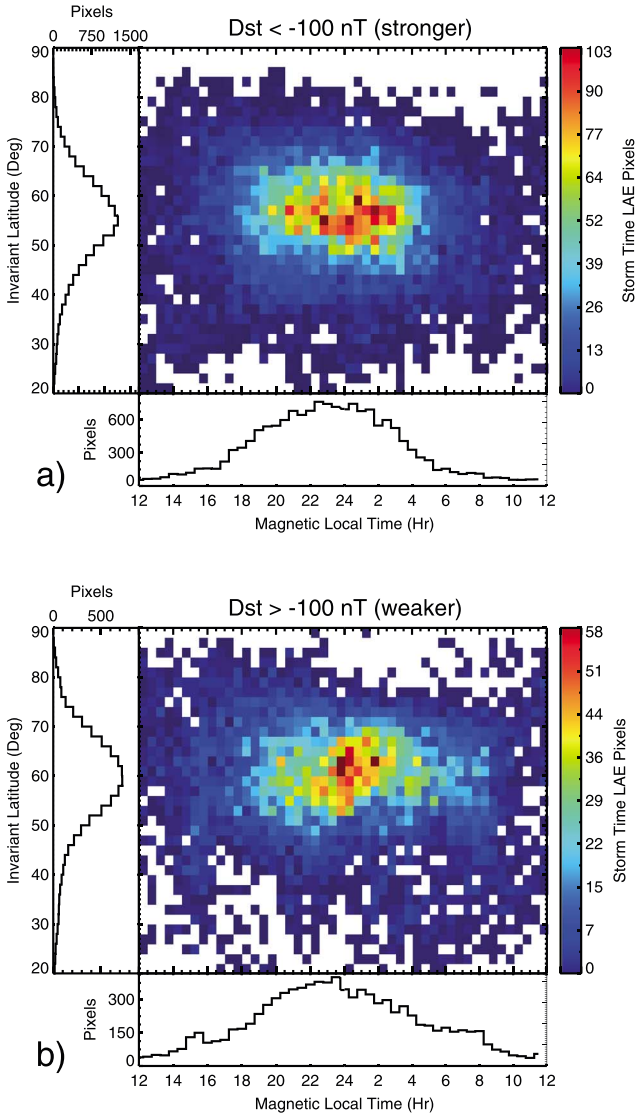

Figure 13. Local time and latitude correlation of LAE pixels for storm time intervals that are (a) <−100 nT (stronger storms) and (b) >−100 nT (weaker storms). Both MLT and IL maintain similarly centered distributions.

similar pattern with stronger storms pushing further into the magnetosphere, leading to lower latitudes. The MLT for both weaker and stronger storms in Figure 13 seem roughly centered slightly dusk of midnight with the weaker storm distribution appearing more spread out in local time.

As discussed in section 2, there could be a potential bias in spatial information simply from irregular sampling due to the GEC. Secondary separate studies of latitude and local time coverage are done using the *satellite location only* to determine if the spatial patterns in Figures 7, 8, and 12 are real or a consequence of some underlying preferential sampling. The idea is to build up a distribution of where the satellite was when it observed a LAE and then evaluate that to see if it behaves similar to the LAE pixel results.

Figure 14 shows the geocentric distance $\left(\sqrt{X_{sm}^2 + Y_{sm}^2}\right)$ along with the Z_{sm} coordinate (north and south together) for all LAE S/C locations. The locations are separated out into times of weaker (>−100 nT)/stronger (<−100 nT) geomagnetic storms, defined by the peak minimum of the main phase. Further out the stronger storm locations (blue dots) are in regions of higher latitude, which translates to lower latitudes (smaller L shells) on the opposite side in MLT. This reinforces the response of IL to *SYM-H* discussed in section 5. (Figure 7.) Stronger storms have a greater chance of having an emission region at lower latitudes. In this context "stronger" indicates an end of main phase with a lower *SYM-H* value. While not always,

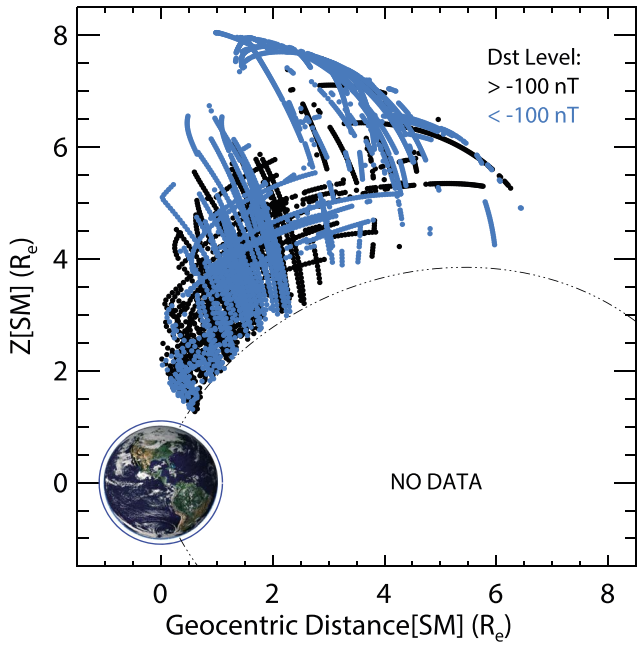

Figure 14. Geocentric distance and *Z* component of all S/C locations in solar magnetic (SM) coordinates when a LAE is observed. Blue dots indicate locations during moderate or stronger storm activity. Locations from ~2–3R_e or further out observe source emissions from the opposite hemisphere. Higher latitudes at the S/C location reflect a lower latitude on the opposite hemisphere.

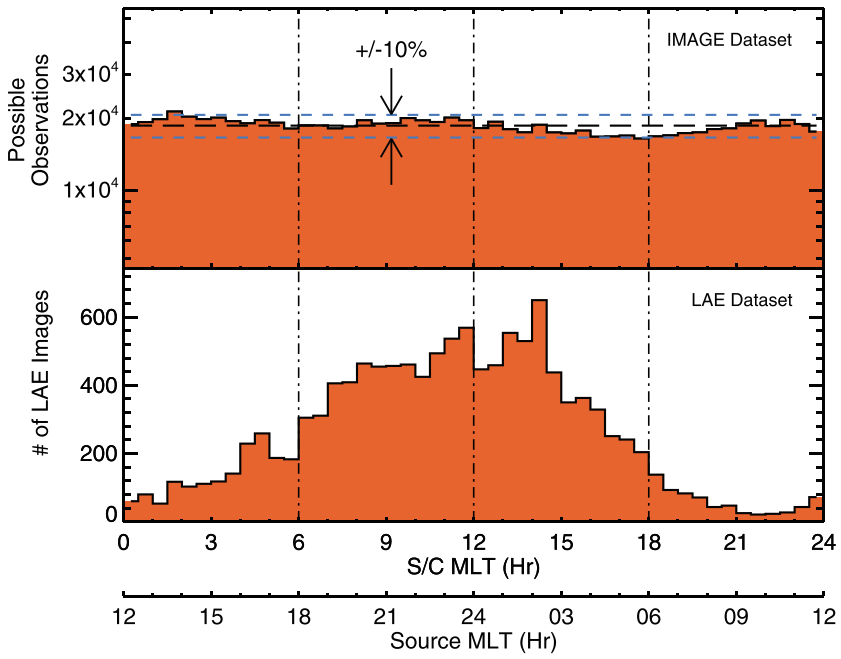

Figure 15. (top) Magnetic local time total possible observation opportunities and (bottom) the observed LAE local time distribution using the S/C location only. The dashed black line in the top plot is the average value over all possible observations with the blue lines set at ±10%. The measurements are directly from the S/C location in SM coordinates. Following the concept of an opposite hemisphere source of a GEC observation, the bottom axis indicates the MLT of the LAE emission.

this can mean a longer, more intense (steeper slope) main phase. The longer the duration of the main phase the more magnetic convection pulls in fresh ions into lower L shells. Further, Figure 14 illustrates a direct observation of the combined GECs over 2000–2005.

To test the local time result using the S/C location, we determine for all data (not just LAE data) how many opportunities are there to possibly be in a specific local time, whether an LAE was observed or not. This is compared to the actual number of observations of LAEs in the same local time bin. Figure 15 summarizes this test with the total number of possible opportunities over the entire IMAGE data set on the top and the actual LAE observations on the bottom. The blue-black-blue dashed lines in the top histogram are the mean and ±10% lines. The total number of possible opportunities as a function of MLT is fairly flat, showing no significant trend. The LAE MLT distribution shows a very similar trend to that in Figure 12, which indicates that the observed spatial distribution in local time is a real result and not just from sampling bias.

7. Discussion/Conclusions

The goal of this study was to establish if escaping Low Altitude Emissions, which are not strictly speaking inside the loss cone, behave the same way as true ion precipitation (i.e., loss to the atmosphere) during varying geomagnetic activity. If so, then it may be possible to observe a single ENA image over the entire local time of the magnetosphere and assess the precipitation region intensity and spatial coverage. This is difficult to prove conclusively because LAEs created by charge exchange leave the ion precipitation population making it difficult to infer any spatial-temporal properties of ions entering the atmosphere. Due to the GEC discussed in section 2, the observed LAEs are a small fraction of the total neutrals created, which in turn are thought to be sourced from the larger ion plasma sheet population before interacting with the atmosphere.

When correlated to the geomagnetic indices *AE*/*Kp*/*SYM-H*, the Low Altitude Emissions appear to respond in a similar manner as ion precipitation regions. In particular the differential directional energy flux increases, the invariant latitude decreases, and the magnetic local time expands in extent. To be precise, the MLT does not statistically correlate. Figure 8 shows the distribution in MLT which appears as a "blob." Instead, what we mean in the context of this discussion is that the dependence on the behavior of the extent in MLT is consistent with changes in ion precipitation regions. All three geomagnetic indices showed a positive increasing correlation with flux, with *SYM-H* showing the most nonlinear response. While the invariant latitude of Low Altitude Emission pixels are the most difficult to characterize due to the uncertainty, we observe a distribution centered roughly at 60° ($L < 4$) with a peak pixel uncertainty of <10°. It is possible that the pitch angle distribution centered above 90° and the invariant latitude near 60° are linked dynamically. Then it could be that the observed LAE distributions in PA/IL are shifted due to multiple charge exchange collisions.

During times of increased geomagnetic activity the IL is seen to reduce significantly, particularly with the *Kp* and *SYM-H* indices. The combined magnetic local time/invariant latitude coverage of observed Low Altitude Emissions appears colocated with ion precipitation regions. In particular, the IL region of LAE pixels lies at 50°–70° ($L = 2.4–8.5$) and indicates a ring current/plasma sheet source. The magnetic local time remains centered roughly dusk of midnight, which is reasonable for the energy range of the Low Altitude Emissions, and appears slightly more spread out during times of greater geomagnetic activity.

Based on the observed response of Low Altitude Emission pixels to geomagnetic activity, we make the following conclusions:

1. The response of Low Altitude Emissions to geomagnetic activity appears most sensitive to the *SYM-H* index.
2. The change in invariant latitude with increasing *SYM-H* follows a similar pattern to ion precipitation of moving to lower L shells.
3. The Low Altitude Emissions studied appear to follow the geomagnetic dynamics and spatial footprints of the ring current. This leads to the conclusion that the population represented here leading to Low Altitude Emissions is a part of the total energy population of the ring current.
4. Additionally, the Low Altitude Emission particles observed in the energy range presented here appears to be from the plasma sheet. This is apparent from the Low Altitude Emission pixel distribution being roughly centered dusk of midnight in an invariant latitude region (~50°–70°) mapping to L shells of ~2.4–8.5.
5. The uncertainty in invariant latitude and magnetic local time due to fixed pixel dimensions in the image do not inhibit the ability to discern changes in ion precipitation spatially.

6. MENA images showing Low Altitude Emissions can be used to access the state of ion precipitation regions during enhanced geomagnetic activity.

This study has shown that while Low Altitude Emissions of Energetic Neutral Atoms are outside the loss cone (in that inside the loss cone means lost to the atmosphere and not able to escape to be detected as ENAs), they perform similarly to ion precipitation regions during storm time.

Appendix A: Computation of Configuration and Velocity Space Values From a MENA Image

A1. Batch Processor

A single MENA image consists of 32 azimuth bins (4°) and 28 in elevation (5°). The azimuth direction (spacecraft (S/C) spin) is along the vertical, and the elevation (instrument field of view) is in the horizontal (Figure A1). A MENA image is a spherical collection of line of sight observations centered on the Earth. The "distance" to each pixel from the center is an angular measurement sigma → σ. It is desired to keep only those pixels that cross the Earth limb at $R_e + h_{em}$ (where the subscript em refers to the emission region), so σ is used as a metric compared to $\sin^{-1}\left(\frac{[R_e+h_{em}]}{r}\right)$, where r is the distance between Earth center and the S/C. Pixels with a nearest corner within this are considered for further processing.

While a single IMAGE orbit has a large eccentricity ranging from an apogee of ~7R_e to a perigee of 1000 km, the actual range of distances of the LAE data set is more like 1.6 to 6 R_e. This means that for a near image (at 1.6 R_e), the angular extent of usable pixels is about 80°, which is roughly 20 (16) pixels in azimuth (elevation) taking up 63% (57%) of an image. Most images are from much further out, and the angular extent is more limited. For an image taken at 6 R_e the angular size of the Earth plus limb is 20°, taking up 5 (4) pixels in azimuth (elevation), or 16% (14%) of an image.

The eventual goal of the batch processor is to compute the solar magnetic (SM) coordinates and magnetic field vector for every usable pixel. To accomplish this, we create a new user-defined coordinate system based on modified spherical coordinates. In this Geocentric Pixel Projection (GPP) system the Z component is centered on the Earth and points toward the S/C. The Y component is aligned with the S/C spin vector, and X completes orthogonality (see Figure A2). In this configuration imagine the emission region as a hemispherical shell projected from the Earth center out toward the IMAGE S/C. The objective of the batch processor is to solve for the spherical angles eta (η) and epsilon (ϵ) for five points (corners and center) of every valid pixel.

The angle epsilon (ϵ), or longitude, is obtained directly from the azimuth and elevation pixel location:

$$\epsilon = \tan^{-1}(\mathrm{az}/\mathrm{el}) \tag{A1}$$

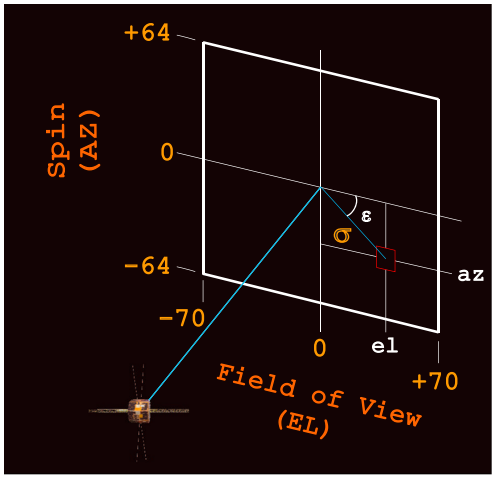

Figure A1. Layout of a MENA ENA image. The long blue line connects the S/C to Earth center. The vertical axis is along the spin direction (azimuth), and the horizontal is the instrument field of view (elevation). The distance in angle from the center of the image is σ, which can be compared to $\sin^{-1}\left(R_e + h_{em}\right)/r$ to determine if the pixel is within a shell of altitude h_{em}. The angle ϵ is the inverse tangent of the pixel location (az/el).

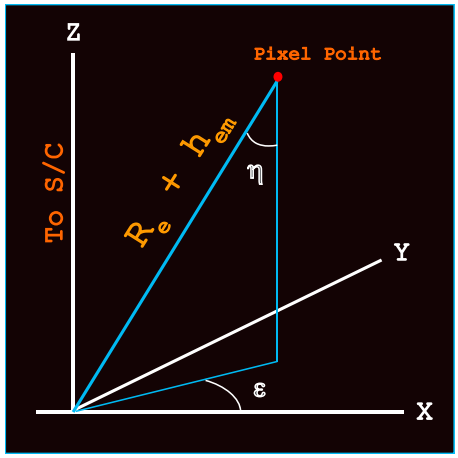

Figure A2. Spherical coordinate orientation of a single pixel point (red dot) assuming the emission is from a spherical shell of radius $R_e + h_{em}$. In the user-defined Geocentric Pixel Projection (GPP) coordinates, the Z axis is from Earth's center to the S/C and the Y axis aligns with the S/C spin axis. The angles eta (η) and epsilon (ϵ) are similar to spherical colatitude and longitude, respectively.

The angle σ used to evaluate the angular distance to a pixel point is also used in the computation of the spherical angles. The blue arc in Figure A3 represents the curved geometry of a MENA image. The actual emission region along the line of sight is somewhere along $\overline{PQ}$ (or further; however, we are limiting this assumption to the realm of Earths magnetospheric influence), but we are assuming it comes from point C. The red line in Figure A3 from the origin to $\perp \overline{PQ}$ is then

$$R\sin(\sigma) \tag{A2}$$

The angle $\angle a$ is then:

$$a = \sin^{-1}\left[\frac{R\sin(\sigma)}{(R_e + h_{em})}\right] \tag{A3}$$

The second spherical angle eta (η), or colatitude, is then obtained by subtracting $(\pi - a)$ from $(\pi - \sigma)$:

$$\eta = (\pi - \sigma) - \left[\pi - \sin^{-1}\left(\frac{R\sin(\sigma)}{R_e + h_{em}}\right)\right] \tag{A4}$$

or simplified

$$\eta = \sin^{-1}\left(\frac{R\sin(\sigma)}{R_e + h_{em}}\right) - \sigma \tag{A5}$$

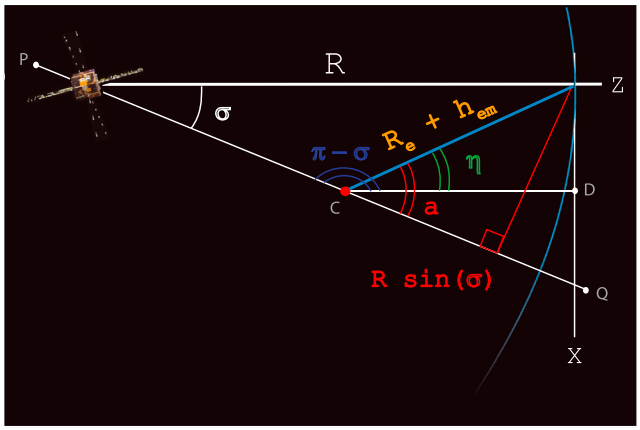

Figure A3. Geometry for computing the spherical coordinates of a pixel point using the satellite location and angular extent of the point on an image. The line of sight integrated ENA flux can have a source region anywhere along $\overline{PQ}$. We assume that this region is on a spherical shell of radius $R_e + h_{em}$ at point C. The angular distance σ in the image (along the blue arc) is used with the assumed radius to compute eta (η).

The final pixel point in GPP coordinates is:

$$\left[\sin(\eta)\cdot(R_e+h_{\mathrm{em}})cos(\epsilon)\,\sin(\eta)\cdot(R_e+h_{\mathrm{em}})sin(\epsilon)\,\cos(\eta)\cdot(R_e+h_{\mathrm{em}})\right]$$

A rotation matrix using the S/C location and spin vector (both in SM coordinates) is applied to a pixel point GPP coordinates, translating it to SM. As a final step, the batch processor uses the International Geomagnetic Reference Field (IGRF-9), [*Macmillan et al.*, 2003] magnetic field model, and the SM coordinates to compute the magnetic field at each pixel point.

A2. Postprocessor

The postprocessor reads in daily data files holding all LAE image information processed by the batch processor. Each image has solar magnetic (SM) coordinates and the magnetic field vector for the five points in every valid pixel. The desired output of the post processor is the magnetic local time (MLT), invariant latitude (IL), and pitch angle (PA) for every valid pixel. To reduce processing, only pixel points within $R_e + h_{\mathrm{em}}$ are considered. The surviving points are used to compute the mean, median, maximum, and minimum values of a pixel. The MLT comes directly from the SM X and Y coordinates:

$$\mathrm{MLT} = 12 + \left(\tan^{-1}\left(\frac{y_{sm}}{x_{sm}}\right)/\pi\right)\times 12 \tag{A6}$$

To determine the IL, the magnetic latitude (ML) must first be calculated using the SM Z coordinate, followed by the L shell value at the emission region:

$$\lambda_{em} = \sin^{-1}\left(\frac{z_{sm}}{\left[R_e+h_{\mathrm{em}}\right]}\right) \tag{A7}$$

$$L = \frac{r}{\cos^2(\lambda_{\mathrm{em}})} \tag{A8}$$

where λ_{em} is the ML and r is in $R_e\left[\frac{(R_e+h_{\mathrm{em}})}{R_e}\right]$, then finally

$$\Lambda = \cos^{-1}\left(\sqrt{\frac{1}{L}}\right) \tag{A9}$$

where Λ is the IL. The pitch angle is defined as the angle between the total velocity vector of a charged particle spiraling about a magnetic field line and the vector direction of the field. The magnitude of the particle velocity is not important, just the direction. If we assume that the ion charge exchanges and keeps its pitch angle at the time of becoming a neutral, then we can use the coordinate information of the emission point and the S/C location to find the velocity vector direction. Similarly, we can use the direction of the magnetic field vector without interest in the magnitude:

$$\alpha = \cos^{-1}\left[\frac{\vec{v}_{\mathrm{ena}}\cdot\vec{B}}{|\,v_{\mathrm{ena}}\,||\,B\,|}\right] \tag{A10}$$

A3. Pitch Angle Filter

To be considered as a valid result, each LAE pixel point should have associated with it a pitch angle that can come from a realistic mirror altitude. Low-altitude estimates of the proton aurora are at ~150 km. This will be our low-altitude limit for a realistic mirror altitude. The pixel emission comes from an assumed top altitude $h_{\mathrm{em}} = 650$ km with an observed pitch angle α_{em}, where the subscript em represents the emission region values. If we assume for a moment a collisionless medium in a simple dipole magnetic field, the first adiabatic invariant states that the magnetic moment at the emission altitude is the same as that of the mirror altitude:

$$\mu_{\mathrm{em}} = \frac{mv_{\perp}^2}{2B} = \mu_{\mathrm{mir}} = \text{constant} \tag{A11}$$

where B is the local magnetic field as a function of altitude, magnetic latitude, and L shell. The pitch angle of a charged particle in a magnetic field is defined by

$$\alpha = \tan^{-1}(v_\perp / v_\parallel) \rightarrow \frac{v_\perp^2}{v_\parallel^2} = \frac{\sin^2 \alpha}{\cos^2 \alpha} \tag{A12}$$

The equation for the local magnetic field assuming a simple dipole is

$$B = \frac{B_o}{R^3}[1 + 3\sin^2 \lambda]^{\frac{1}{2}} \tag{A13}$$

where λ is the magnetic latitude at some altitude and R is the Earth-centered variable distance ($R_e + h$). The magnetic latitude is a function of the L shell and can be written in terms of the invariant latitude (latitude at $L = 1$, corresponding to $r = R_e$):

$$\begin{aligned} \lambda &= \cos^{-1}\left(\frac{r}{L}\right)^{\frac{1}{2}} \\ L &= \frac{1}{\cos^2(\Lambda)} \end{aligned} \tag{A14}$$

where r is in R_e and Λ is the invariant latitude. Combined, the magnetic latitude is then

$$\begin{aligned} \lambda &= \cos^{-1}\left[\frac{(R_e + h)}{R_e L}\right]^{\frac{1}{2}} \\ \lambda &= \cos^{-1}\left[\frac{(R_e + h)}{R_e}\cos^2 \Lambda\right]^{\frac{1}{2}} \end{aligned} \tag{A15}$$

The magnetic field at some variable altitude h as a function of invariant latitude is then

$$B = \frac{B_o}{(R_e + h)^3}\left[1 + 3\sin^2\left(\cos^{-1}\left[\frac{(R_e + h)}{R_e}\cos^2 \Lambda\right]^{\frac{1}{2}}\right)\right]^{\frac{1}{2}} \tag{A16}$$

The first adiabatic invariant can then be written in terms of the pitch angle:

$$\mu = \frac{\frac{1}{2}mv_\perp^2}{B} \propto \frac{v_\perp^2}{B} \propto \frac{\sin^2 \alpha}{B} \tag{A17}$$

This leads to an expression for the pitch angle at a different magnetic field, given the emission pitch angle and magnetic field:

$$\alpha = \sin^{-1}\frac{\sin^2 \alpha_{\text{em}}}{B_{\text{em}}}B \tag{A18}$$

Combining everything together gives an equation for the pitch angle at an altitude h given the emission magnetic latitude (computed from the invariant latitude at an altitude $h_{\text{em}} = 650$ km, $R_e + h_{\text{em}} = 7020$ km) and emission pitch angle:

$$\alpha = \sin^{-1}\left[\frac{\sin^2 \alpha_{\text{em}}}{(R_e + h)^3\left[1 + 3\sin^2 \lambda_{\text{em}}\right]^{\frac{1}{2}}}(7020)^3\left[1 + 3\sin^2\left(\cos^{-1}\left[\frac{(R_e + h)}{R_e}\cos^2 \Lambda\right]^{\frac{1}{2}}\right)\right]^{\frac{1}{2}}\right]^{\frac{1}{2}} \tag{A19}$$

A profile of the computed pitch angle as a function of altitude is generated for different magnetic latitudes (Figure 3). The altitude h in which the pitch angle is ~90° is then the mirror altitude. If the mirror altitude is above 150 km, then the pixel point is considered valid.

Acknowledgments
We are thankful for the many talented people at SwRI for their wisdom. This work was supported at SwRI under NASA grant NNX10-AL21G. IMAGE MENA data can be found at http://guinan.space.swri.edu/IMAGE/.

References

Basu, B., J. R. Jasperse, R. M. Robinson, R. R. Vondrak, and D. S. Evans (1987), Linear transport theory of auroral proton precipitation—A comparison with observations, *J. Geophys. Res.*, *92*, 5920–5932, doi:10.1029/JA092iA06p05920.

Bazell, D., E. C. Roelof, T. Sotirelis, P. C. Brandt, H. Nair, P. Valek, J. Goldstein, and D. McComas (2010), Comparison of TWINS images of low-altitude emission of energetic neutral atoms with DMSP precipitating ion fluxes, *J. Geophys. Res.*, *115*, A10204, doi:10.1029/2010JA015644.

Brandt, P. C. ., S. Barabash, O. Norberg, R. Lundin, E. C. Roelof, C. J. Chase, B. H. Mauk, and M. Thomsen (1997), ENA imaging from the Swedish micro satellite Astrid during the magnetic storm of 8 February, 1995, *Adv. Space Res.*, *20*, 1061–1066.

Brandt, P. C., S. Barabash, E. C. Roelof, and C. J. Chase (2001a), Energetic neutral atom imaging at low altitudes from the Swedish microsatellite Astrid: Observations at low (≤10 keV) energies, *J. Geophys. Res.*, *106*, 24,663–24,674, doi:10.1029/2000JA900119.

Burch, J. L. (2000), IMAGE mission overview, *Space Sci. Rev.*, *91*, 1–14.

Buzulukova, N., M.-C. Fok, E. Roelof, J. Redfern, J. Goldstein, P. Valek, and D. McComas (2013), Comparative analysis of low-altitude ENA emissions in two substorms, *J. Geophys. Res. Space Physics*, *118*, 724–731, doi:10.1002/jgra.50103.

Colier, M., D. Chornay, J. Clemmons, J. Keller, J. Klenzing, J. Kujawski, J. McLain, R. Pfaff, D. Rowland, and M. Zettergren (2015), VISIONS remote observations of a spatially-structured filamentary source of energetic neutral atoms near the polar cap boundary during an auroral substorm, *Adv. Space Res.*, *56*(10), 2097–2105.

Daglis, I. A., R. M. Thorne, W. Baumjohann, and S. Orsini (1999), The terrestrial ring current: Origin, formation, and decay, *Rev. Geophys.*, *37*, 407–438, doi:10.1029/1999RG900009.

Dessler, A. J., and E. N. Parker (1959), Hydromagnetic theory of geomagnetic storms, *J. Geophys. Res.*, *64*, 2239–2252, doi:10.1029/JZ064i012p02239.

Eather, R. H. (1967), Auroral proton precipitation and hydrogen emissions, *Rev. Geophys.*, *5*, 207–285, doi:10.1029/RG005i003p00207.

Ebihara, Y., M. Ejiri, and H. Miyaoka (1998), Simulation on ring current formation: A case study of a storm on February 13, 1972, in *Proceedings of the NIPR Symposium on Upper Atmosphere Physics, No. 12. December, 1998. Papers presented at the 21st Symposium on Coordinated Observations of the Ionosphere and the Magnetosphere in the Polar Regions held 24-25 July, 1997 at NIPR, Tokyo*, vol. 12, edited by H. Yamagishi, pp. 1–11, Natl. Inst. Polar Res., Tokyo.

Ebihara, Y., and M. Ejiri (2000), Simulation study on fundamental properties of the storm-time ring current, *J. Geophys. Res.*, *105*, 15,843–15,860, doi:10.1029/1999JA900493.

Fok, M.-C., T. E. Moore, and M. E. Greenspan (1996), Ring current development during storm main phase, *J. Geophys. Res.*, *101*, 15,311–15,322, doi:10.1029/96JA01274.

Frey, H. U., S. B. Mende, T. J. Immel, J.-C. Gérard, B. Hubert, S. Habraken, J. Spann, G. R. Gladstone, D. V. Bisikalo, and V. I. Shematovich (2003), Summary of quantitative interpretation of IMAGE far ultraviolet auroral data, *Space Sci. Rev.*, *109*, 255–283, doi:10.1023/B:SPAC.0000007521.39348.a5.

Galand, M., and S. Chakrabarti (2006), Proton aurora observed from the ground, *J. Atmos. Sol. Terr. Phys.*, *68*, 1488–1501, doi:10.1016/j.jastp.2005.04.013.

Galand, M., and D. Lummerzheim (2004), Contribution of proton precipitation to space-based auroral FUV observations, *J. Geophys. Res.*, *109*, A03307, doi:10.1029/2003JA010321.

Galand, M., and A. D. Richmond (1999), Magnetic mirroring in an incident proton beam, *J. Geophys. Res.*, *104*, 4447–4456, doi:10.1029/1998JA900123.

Galand, M., and A. D. Richmond (2001), Ionospheric electrical conductances produced by auroral proton precipitation, *J. Geophys. Res.*, *106*, 117–126, doi:10.1029/1999JA002001.

Galand, M., J. Lilensten, W. Kofman, and D. Lummerzheim (1998), Proton transport model in the ionosphere: 2. Influence of magnetic mirroring and collisions on the angular redistribution in a proton beam, *Ann. Geophys.*, *16*, 1308–1321, doi:10.1007/s00585-998-1308-y.

Gérard, J.-C., B. Hubert, M. Meurant, V. I. Shematovich, D. V. Bisikalo, H. Frey, S. Mende, G. R. Gladstone, and C. W. Carlson (2001), Observation of the proton aurora with IMAGE FUV imager and simultaneous ion flux in situ measurements, *J. Geophys. Res.*, *106*, 28,939–28,948, doi:10.1029/2001JA900119.

Goldstein, J., D. J. McComas, P. Valek, J. Redfern, F. Søraas, and D. Bazell (2013), Local-time-dependent low-altitude ion spectra deduced from TWINS ENA images, *J. Geophys. Res. Space Physics*, *118*, 2928–2950, doi:10.1002/jgra.50222.

Gussenhoven, M. S., D. A. Hardy, and N. Heinemann (1987), The equatorward boundary of auroral ion precipitation, *J. Geophys. Res.*, *92*, 3273–3283, doi:10.1029/JA092iA04p03273.

Hardy, D. A., M. S. Gussenhoven, and D. Brautigam (1989), A statistical model of auroral ion precipitation, *J. Geophys. Res.*, *94*, 370–392, doi:10.1029/JA094iA01p00370.

Henderson, M. G., G. D. Reeves, H. E. Spence, R. B. Sheldon, A. M. Jorgensen, J. B. Blake, and J. F. Fennell (1997), First energetic neutral atom images from Polar, *Geophys. Res. Lett.*, *24*, 1167–1170, doi:10.1029/97GL01162.

Hedin, A. E. (1991), Extension of the MSIS thermosphere model into the middle and lower atmosphere, *J. Geophys. Res.*, *96*, 1159–1172, doi:10.1029/90JA02125.

Hovestadt, D., B. Häusler, and M. Scholer (1972), Observation of energetic particles at very low altitudes near the geomagnetic equator, *Phys. Rev. Lett.*, *28*, 1340–1344, doi:10.1103/PhysRevLett.28.1340.

Hultqvist, B. (1971), On the production of a magnetic-field-aligned electric field by the interaction between the hot magnetospheric plasma and the cold ionosphere, *Planet. Space Sci.*, *19*, 749–759, doi:10.1016/0032-0633(71)90033-X.

Ilie, R., R. M. Skoug, H. O. Funsten, M. W. Liemohn, J. J. Bailey, and M. Gruntman (2013), The impact of geocoronal density on ring current development, *J. Atmos. Sol. Terr. Phys.*, *99*, 92–103, doi:10.1016/j.jastp.2012.03.010.

Jordanova, V. K., C. J. Farrugia, J. M. Quinn, R. M. Thorne, K. E. Ogilvie, R. P. Lepping, G. Lu, A. J. Lazarus, M. F. Thomsen, and R. D. Belian (1998), Effect of wave-particle interactions on ring current evolution for January 10–11, 1997: Initial results, *Geophys. Res. Lett.*, *25*, 2971–2974, doi:10.1029/98GL00649.

Jordanova, V. K., R. B. Torbert, R. M. Thorne, H. L. Collin, J. L. Roeder, and J. C. Foster (1999b), Ring current activity during the early $B_z < 0$ phase of the January 1997 magnetic cloud, *J. Geophys. Res.*, *104*, 24,895–24,914, doi:10.1029/1999JA900339.

Jordanova, V. K., C. J. Farrugia, R. M. Thorne, G. V. Khazanov, G. D. Reeves, and M. F. Thomsen (2001), Modeling ring current proton precipitation by electromagnetic ion cyclotron waves during the May 14–16, 1997, storm, *J. Geophys. Res.*, *106*, 7–22, doi:10.1029/2000JA002008.

Jorgensen, A. M., H. E. Spence, M. G. Henderson, G. D. Reeves, M. Sugiura, and T. Kamei (1997), Global Energetic Neutral Atom (ENA) measurements and their association with the *Dst* index, *Geophys. Res. Lett.*, *24*, 3173–3176, doi:10.1029/97GL03095.

Kistler, L. M., F. M. Ipavich, D. C. Hamilton, G. Gloeckler, and B. Wilken (1989), Energy spectra of the major ion species in the ring current during geomagnetic storms, *J. Geophys. Res.*, *94*, 3579–3599, doi:10.1029/JA094iA04p03579.

Korth, H., M. F. Thomsen, J. E. Borovsky, and D. J. McComas (1999), Plasma sheet access to geosynchronous orbit, *J. Geophys. Res.*, *104*, 25,047–25,062, doi:10.1029/1999JA900292.

Kozelov, B. V. (1993), Influence of the dipolar magnetic field on transport of proton-H atom fluxes in the atmosphere, *Ann. Geophys.*, *11*, 697–704.

Kozyra, J. U., M.-C. Fok, E. R. Sanchez, D. S. Evans, D. C. Hamilton, and A. F. Nagy (1998a), The role of precipitation losses in producing the rapid early recovery phase of the Great Magnetic Storm of February 1986,*J. Geophys. Res.*, *103*, 6801–6814, doi:10.1029/97JA03330.

Kozyra, J. U., M. W. Liemohn, C. R. Clauer, A. J. Ridley, M. F. Thomsen, J. E. Borovsky, J. L. Roeder, V. K. Jordanova, and W. D. Gonzalez (2002), Multistep *Dst*development and ring current composition changes during the 4–6 June 1991 magnetic storm, *J. Geophys. Res.*, *107*(A8), 1224, doi:10.1029/2001JA000023.

Liemohn, M. W., J. U. Kozyra, M. F. Thomsen, J. L. Roeder, G. Lu, J. E. Borovsky, and T. E. Cayton (2001), Dominant role of the asymmetric ring current in producing the stormtime *Dst**, *J. Geophys. Res.*, *106*, 10,883–10,904, doi:10.1029/2000JA000326.

Lui, A. T. Y., and C. D. Anger (1973), A uniform belt of diffuse auroral emission seen by the ISIS-2 scanning photometer, *Planet. Space Sci.*, *21*, 799–809, doi:10.1016/0032-0633(73)90097-4.

Lui, A. T. Y., P. Perreault, S.-I. Akasofu, and C. D. Anger (1973), The diffuse aurora, *Planet. Space Sci.*, *21*, 857, doi:10.1016/0032-0633(73)90102-5.

Lui, A. T. Y., C. D. Anger, and S.-I. Akasofu (1975), The equatorward boundary of the diffuse aurora and auroral substorms as seen by the Isis 2 auroral scanning photometer,*J. Geophys. Res.*, *80*, 3603–3614, doi:10.1029/JA080i025p03603.

Macmillan, S., et al. (2003), The 9th-generation international geomagnetic reference field, *Geophy. J. Int.*, *155*, 1051–1056, doi:10.1111/j.1365-246X.2003.02102.x.

McComas, D. J., et al. (2009a), The Two Wide-angle Imaging Neutral-atom Spectrometers (TWINS) NASA mission-of-opportunity, *Space Sci. Rev.*, *142*, 157–231, doi:10.1007/s11214-008-9467-4.

Meinel, A. B. (1951), Doppler-shifted auroral hydrogen emission, *Astrophys. J.*, *113*, 50, doi:10.1086/145375.

Mende, S. B., H. U. Frey, T. J. Immel, J.-C. Gerard, B. Hubert, and S. A. Fuselier (2003), Global imaging of proton and electron aurorae in the far ultraviolet, *Space Sci. Rev.*, *109*, 211–254, doi:10.1023/B:SPAC.0000007520.23689.08.

Mitchell, D. G., et al. (2000), High Energy Neutral Atom (HENA) imager for the IMAGE mission, *Space Sci. Rev*, *91*, 67–112.

Moore, T. E., et al. (2000), The low-energy neutral atom imager for IMAGE, *Space Sci. Rev.*, *91*, 155–195.

Moritz, J. (1972), Energetic protons at low equatorial altitudes, *Z. Geophys.*, *38*, 701–717.

Newell, P. T., C.-I. Meng, E. R. Sanchez, W. J. Burke, and M. E. Greenspan (1991), Identification and observations of the plasma mantle at low altitude, *J. Geophys. Res.*, *96*, 35–45, doi:10.1029/90JA01760.

Parks, G. K. (2004), *Physics of Space Plasmas: An Introduction*, Westview Press, Boulder, Colo.

Perez, J. D., E. W. Grimes, J. Goldstein, D. J. McComas, P. Valek, and N. Billor (2012), Evolution of CIR storm on 22 July 2009, *J. Geophys. Res.*, *117*, A09221, doi:10.1029/2012JA017572.

Pollock, C. J., et al. (2000), Medium Energy Neutral Atom (MENA) imager for the IMAGE mission, *Space Sci. Rev.*, *91*, 113–154.

Pollock, C. J., A. Isaksson, J.-M. Jahn, F. Søraas, and M. Sørbø (2009), Remote global-scale observations of intense low-altitude ENA emissions during the Halloween geomagnetic storm of 2003, *Geophys. Res. Lett.*, *36*, L19101, doi:10.1029/2009GL038853.

Roelof, E. C. (1987), Energetic neutral atom image of a storm-time ring current, *Geophys. Res. Lett.*, *14*, 652–655, doi:10.1029/GL014i006p00652.

Roelof, E. C. (1997), ENA emission from nearly-mirroring magnetospheric ions interacting with the exosphere, *Adv. Space Res.*, *20*, 361–366, doi:10.1016/S0273-1177(97)00692-3.

Roelof, E. C., and A. J. Skinner (2000), Extraction of ion distributions from magnetospheric ENA and EUV images, *Space Sci. Rev.*, *91*, 437–459.

Roelof, E. C., D. G. Mitchell, and D. J. Williams (1985), Energetic neutral atoms (*E* approximately 50 keV) from the ring current—IMP 7/8 and ISEE 1, *J. Geophys. Res.*, *90*, 10,991–11,008, doi:10.1029/JA090iA11p10991.

Senior, C., J. R. Sharber, J. D. Winningham, O. de La Beaujardiere, R. A. Heelis, D. S. Evans, M. Sugiura, and W. R. Hoegy (1987), *E* and *F* region study of the evening sector auroral oval—A Chatanika/Dynamics Explorer 2/NOAA 6 comparison, *J. Geophys. Res.*, *92*, 2477–2494, doi:10.1029/JA092iA03p02477.

Søraas, F., and K. Aarsnes (1996), Observations of ENA in and near a proton arc, *Geophys. Res. Lett.*, *23*, 2959–2962, doi:10.1029/96GL02821.

Søraas, F., and M. Sørbø (2013), Low altitude observations of ENA from the ring current and from the proton oval, *J. Atmos. Sol. Terr. Phys.*, *99*, 104–110, doi:10.1016/j.jastp.2012.10.003.

Söraas, F., H. R. Lindalen, K. Måseide, A. Egeland, T. A. Sten, and D. S. Evans (1974), Proton precipitation and the Hβ emission in a postbreakup auroral glow, *J. Geophys. Res.*, *79*, 1851–1859, doi:10.1029/JA079i013p01851.

Valek, P., P. C. Brandt, N. Buzulukova, M.-C. Fok, J. Goldstein, D. J. McComas, J. D. Perez, E. Roelof, and R. Skoug (2010), Evolution of low-altitude and ring current ENA emissions from a moderate magnetospheric storm: Continuous and simultaneous TWINS observations, *J. Geophys. Res.*, *115*, A11209, doi:10.1029/2010JA015429.

Vorobjev, V. G., and O. I. Yagodkina (2014), Comparative characteristics of ion and electron precipitation in the dawn and dusk sectors, *Geomag. Aeron.*, *54*, 50–58, doi:10.1134/S0016793214010162.

Williams, D. J. (1987), Ring current and radiation belts, *Rev. Geophys.*, *25*, 570–578, doi:10.1029/RG025i003p00570.

Williams, D. J., E. C. Roelof, and D. G. Mitchell (1992), Global magnetospheric imaging, *Rev. Geophys.*, *30*, 183–208, doi:10.1029/92RG00732.

Winningham, J. D., J. L. Burch, and R. A. Frahm (1984), Bands of ions and angular V's—A conjugate manifestation of ionospheric ion acceleration, *J. Geophys. Res.*, *89*, 1749–1754, doi:10.1029/JA089iA03p01749.

Yagodkina, O. I., and V. G. Vorobjev (2002), Global distribution of auroral proton precipitation inferred from the DMSP data, in *Physics of Auroral Phenomena, Proc. XXXV Annual Seminar, Apatity*, pp. 123–126, Kola Science Centre, Russian Academy of Science, Apatity, Murmansk, Russia.